Article:
Fry-Bouriaux, L, Rosamond, MC, Williams, DA et al. (2 more authors) (2017) Field-enhanced direct tunneling in ultrathin atomic-layer-deposition-grown Au-Al2O3-Cr metal-insulator-metal structures. Physical Review B - Condensed Matter and Materials Physics, 96 (11). 115435. ISSN 1098-0121

https://doi.org/10.1103/PhysRevB.96.115435

Field-enhanced direct tunneling in ultrathin atomic-layer-deposition-grown Au-Al_2O_3-Cr metal-insulator-metal structures

L. Fry-Bouriaux,[1,2] M. C. Rosamond,[1] D. A. Williams,[2] A. G. Davies,[1] and C. Wälti[1]
[1]*Institute of Microwaves and Photonics, School of Electronic and Electrical Engineering, University of Leeds, Leeds LS2 9JT*
[2]*Hitachi Cambridge Laboratory, J.J. Thomson Avenue, Cambridge CB3 0HE*
(Received 4 May 2017; published 19 September 2017)

Metal-insulator-metal structures based on ultrathin high-*k* dielectric films are underpinning a rapidly increasing number of devices and applications. Here, we report detailed electrical characterizations of asymmetric metal-insulator-metal devices featuring atomic layer deposited 2-nm-thick Al_2O_3 films. We find a high consistency in the current density as a function of applied electric field between devices with very different surface areas and significant asymmetries in the *IV* characteristics. We show by TEM that the thickness of the dielectric film and the quality of the metal-insulator interfaces are highly uniform and of high quality, respectively. In addition, we develop a model which accounts for the field enhancement due to the small sharp features on the electrode surface and show that this can very accurately describe the observed asymmetry in the current-voltage characteristic, which cannot be explained by the difference in work function alone.

DOI: 10.1103/PhysRevB.96.115435

I. INTRODUCTION

Thin films of high dielectric constant materials (high-*k* dielectrics) deposited by atomic layer deposition (ALD) are becoming increasingly important in a number of technological areas that require dielectric materials with high quality and uniformity over large surface areas. Using ALD it is possible to deposit uniform-thickness, pinhole-free, conformal, highly reproducible metal-oxide thin films over large surface areas, making it particularly promising with regard to mass fabrication of capacitors and devices based on tunneling. For example, metal-insulator-metal (MIM) capacitors with ALD deposited high-*k* dielectrics are used in applications such as radio-frequency (RF) capacitors for integrated circuits [1–4] and storage capacitors for dynamic RAM (DRAM) [5]. Similarly, MIM diodes critically underpin high-speed electronics applications such as infrared (IR) detectors [6–8] used in energy harvesting applications and backplane selector diodes for LCD displays. In addition, ultrathin ALD deposited oxides are also being explored for use in emerging applications such as metallic single-electron devices [9] (SEDs) including single-electron transistors (SETs) for nonvolatile memory (NVM) applications [10,11].

Conventional metallic SET systems require very small junction areas to reduce the capacitance and an insulating film thin enough, usually on the order of 1 nm for Al_2O_3, such that direct tunneling occurs and is the dominant process. The symmetry and linearity of the MIM device current-voltage (*IV*) curve are important design factors affecting the properties of an SET system and particularly superlattice systems [12]. In rectenna systems opposing requirements are imposed on the MIM device, where high asymmetry and nonlinearity of the *IV* curve are highly desirable in the direct tunneling regime [13]. These devices must also have very high cutoff frequencies reaching the optical part of the spectrum [14] which requires an optimum balance of the junction resistance and capacitance. It is critical, therefore, for both of these applications that there is a small junction area to produce a small capacitance and that the films are thin enough to allow direct tunneling as well as producing the particular features of the *IV* curve such as its asymmetry.

Despite the widespread applications of ALD deposited thin films, the relation between the surface morphology and the symmetry and linearity of the *IV* characteristics of MIM devices is poorly understood, in particular in devices employing ALD-deposited ultrathin dielectric films with thickness below 5 nm. This presents significant challenges for engineering and manufacturing of MIM devices with specific symmetry requirements in their tunneling characteristics.

An ideal MIM structure is shown in Fig. 1(a). In a MIM device fabrication process, metal electrodes are typically evaporated onto a substrate, with the roughness of such evaporated thin films dependent on the thickness and deposition rate [15,16], amongst other factors. Effects of field enhancement on the tunneling characteristics of thicker MIM devices with large surface areas are well studied in the context of Fowler-Nordheim tunneling [17]. Alimardani *et al.* investigated the effect of roughness of the bottom electrode [4] and concluded that the rough surface of metals deposited by evaporation can cause an inversion of the forward bias configuration due to field enhancement at roughness peaks and that structures designed to be symmetric show asymmetry due to this effect. More recently Lau *et al.* have reported that the roughness-smoothing effect in the Al_2O_3 ALD process [18], which leads to the top electrode having a smoother interface with the oxide than the bottom electrode, enhances the asymmetry in the *IV* characteristics. In the Fowler-Nordheim tunneling regime, effects of field enhancement are known to play an important role as the tunnel current is much more sensitive to the shape of the potential barrier [17] than in the direct tunneling regime. However, field enhancement can still play an important role in the direct tunneling regime of MIM devices employing ALD-deposited dielectric films, which is the subject of this paper.

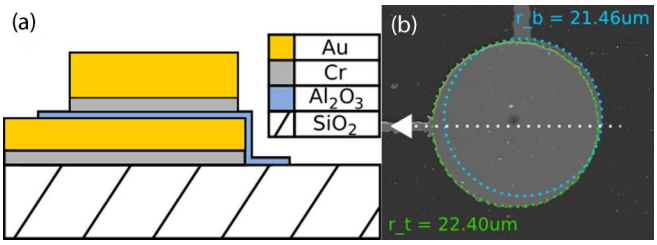

FIG. 1. (a) Schematic of the cross section of a typical MIM structure. (b) SEM image of the 40 μm device, highlighting the measured radii of the bottom (blue) and top (green) electrodes.

Here, we present the detailed electronic characterization together with transmission electron microscopy analysis of MIM devices featuring a 2-nm-thick ALD deposited film and surface areas of 40 μm and 80 μm diameter disks. Figure 1(b) shows an SEM image of a 40 μm device. In order to understand the features of the *IV* curves in detail over the whole bias range, we developed a model that takes into account the asymmetric roughness caused by the aforementioned smoothing effect. The model complements Miller *et al.*'s symmetric roughness model [19] that considers thickness fluctuations but doesn't consider field enhancement. Our model successfully reproduces the experimentally observed asymmetry and is highly consistent with the measured *IV* characteristics over a wide bias range.

II. EXPERIMENTAL DETAILS

The MIM devices were fabricated on 500-μm-thick quartz substrates. The devices are formed by a stacked structure with large disks as electrodes with various diameters to yield a wide range of current densities and capacitances. A circular structure was employed to ensure the electric fringe-field strength is minimized and one electrode was made slightly larger to account for optical alignment errors. Figure 1(a) shows a schematic of the cross section detailing the various layers of the device and Fig. 1(b) shows an SEM image of one of the devices investigated in this paper. The substrates were first cleaned in water, acetone, and then IPA by sonication. The bottom electrodes were formed using optical lithography with a LOR-3A/S1813 photoresist bilayer to ensure good undercut. A 5 nm/25 nm chromium/gold layer was deposited using a Leybold electron-beam evaporation system and liftoff performed using 1165 Remover and further solvent cleaning afterwards. Only very thin electrodes were deposited and at a low deposition rate (<1 nm/s) to reduce roughness as much as possible.

The dielectric layer was then deposited by ALD using the TMA/O_2-plasma method at 200 °C. The ALD system used was a CambridgeNanotech Fiji with load lock. The growth rate was determined using SiO_2 on silicon substrates. 200 ALD cycles were deposited, and subsequently an etch mask was defined using standard optical lithography, after which the ALD film was wet etched in 100 °C orthophosphoric acid. Finally the step height was measured by AFM. The growth per cycle (GPC) was found to be 0.114 nm/cycle. The films for both types of devices were deposited by running 18 cycles to produce a thickness close to 2 nm. The film thickness was estimated by TEM to a resolution of 0.1 nm. The ALD O_2-plasma source was used to clean the samples in the chamber, for two minutes at 200 °C and 300 W.

Once the dielectric films were deposited, cleaning by sonication was avoided as the films are fragile when deposited on gold. Wet etching in 100 °C orthophosphoric acid was used to clear the edges of the bottom electrodes of covering Al_2O_3 for the contact pads. S1813 baked at 115 °C was used as an etch mask, and the measured etch rate of the thin film was roughly 2 nm/min. The top electrode masks were formed using optical lithography with a PMMA/S1813 bilayer. A thick PMMA layer baked at a high temperature protects the underlying oxide from the S1813 developer. A UVO cleaner was used as a source of UV radiation to expose the PMMA, which was developed using undiluted MIBK after patterning the S1813 layer. A chromium/gold layer of thickness 5 nm/65 nm was then deposited to form the top electrode. The large thickness was chosen to ensure continuity over the step caused by the bottom electrode and the deposited dielectric. Contact pads were then deposited, formed of 5 nm Cr/120 nm Au, and the devices glued to a ceramic chip package using a high thermal conductivity varnish. Finally, the devices were wirebonded and inspected by optical microscopy to check for visible faults.

The *IV* characteristics of the MIM devices were measured using a Keithley 2400LV Source-Meter to source voltage and measure current in a two-port configuration. The device is shielded and the shield connected to the earth connection of the source meter so that fully shielded connections can be made to the device. The maximum ADC integration time of the source meter was used and 10 cycles of averaging were performed to reduce noise further in the measurements. A slowly-changing offset current between $\pm$100 pA was present at zero bias depending on the source meter used, which is a negligible contribution to the data presented here. The TEM sample for the cross section analysis was prepared using a Ga ion milling process and stored under vacuum. TEM/STEM/EDX was performed using an FEI Titan Themis system.

III. DEVICE CHARACTERIZATION

The current density as a function of the electric field for the 40 μm (D_1) and the 80 μm diameter device (D_2) are shown in Fig. 2 in orange and blue, respectively. The bottom electrode of the MIM structure is used as the ground reference potential. The current density is derived using $J = I/A$ where A is the electrode area and I the measured current, and the electric field was derived using $E = V_B/t$ where $t = 2$ nm is the measured thickness of the film and V_B the applied voltage across the MIM structure. For the device D_1 shown in Fig. 1(b), the area A was obtained by finding the offset between the circle centres and computing the area intersected by these circles. For device D_2 (shown in the Supplemental Material [20]) the area A is defined by the top electrode area. The overlap of the two curves in the current density plot shows that the consistency between these two devices is very high despite using a simple parallel plate geometry. This implies that the typical length scale of the geometrical imperfections on the electrode surface that impact the *IV* characteristics must be much smaller than the electrode surface area of both devices.

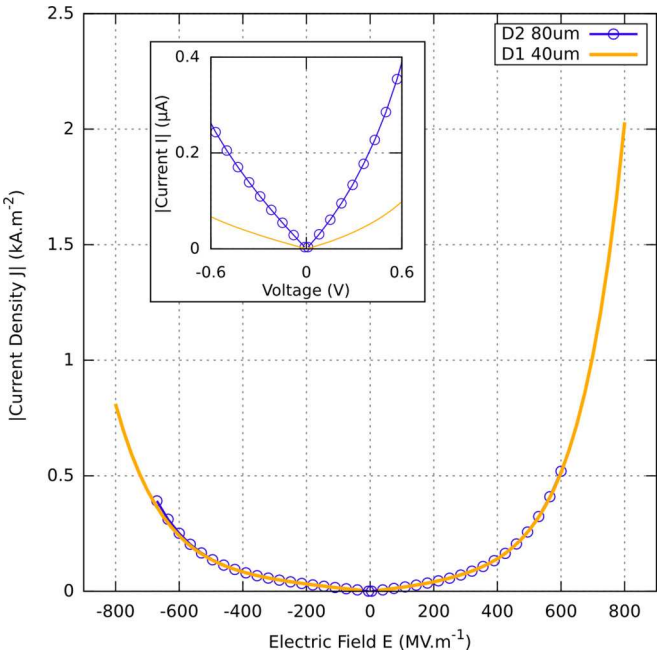

FIG. 2. Current density (J) versus electric field (E) curves for devices D_1 (40 μm diameter) and D_2 (80 μm diameter) at room temperature. The inset shows the IV characteristics of the same devices between -0.6 V and 0.6 V.

Figure 3 shows a representative TEM image in which the MIM structure is clearly visible and the different layers can be identified, allowing an accurate estimation of the oxide thickness and interfacial quality to be made. Additional TEM images similar to those presented here are included in the Supplemental Material [20]. In the region highlighted by the red ellipse, there is minimal transverse variation of the structure and the nanoscale structure of all the materials is visible. The top and bottom electrode Au grain structure is columnar and the bottom Au surface is minimally rough relative to the thickness of the Al_2O_3 film in large portions of the area. The Al_2O_3 film is clearly uniform and conformal, and the thickness measures very close to 2.0 nm within 0.1 nm. The

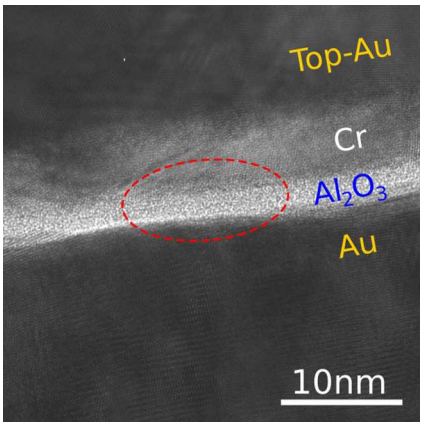

FIG. 3. Large area TEM image showing all compounds of the MIM structure. The uniformity of the Al_2O_3 layer and its amorphous structure are clearly visible.

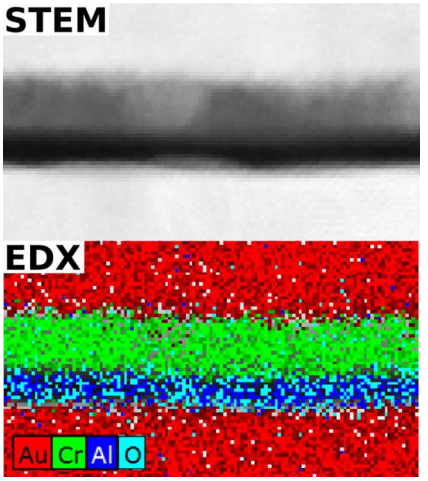

FIG. 4. STEM image and corresponding EDX data showing strong and clear signals for Au shown in red, Cr in green, and Al in blue. The oxygen signal is more noisy and is shown in turquoise. The material interfaces appear to be very sharp.

observed uniformity of the thickness obtained demonstrates that the ALD growth was linear within very few cycles on both SiO_2 and Au. This implies that the Au surface had enough reactive sites for the nucleation delay in the initial stages of growth to be negligible. This may be due to impurities on the surface and the *in situ* oxygen plasma ashing step where oxygen radicals may be adsorbed at vacancies on the bottom Au surface [21,22] with sufficient density for the surface to be saturated with TMA precursor molecules.

STEM/EDX imaging was performed in a number of areas of the MIM structure to confirm material consistency. The bottom panel in Fig. 4 shows a mapping of EDX signals over the region shown in the STEM image in the top panel of Fig. 4. The Au, Cr, and Al signals are strong and clearly discernible, indicating that all the materials are homogeneous. However, the O signal is noisy and appears prominently not only in the Al_2O_3 region, but also in the entire Cr layer. This is likely due to the significant overlap of the O-K peak centered at 532 eV and the edge of the Cr-L_3 peak centered at 575 eV that has a delayed maximum (EELS Atlas data [23]), leading to false signals for oxygen in the Cr layer. We note that while it is conceivable that oxygen may diffuse from the Al_2O_3 into the Cr layer, this would result in a visible change of the Cr structure predominately at the interface, which is inconsistent with the homogeneous distribution of O in the Cr layer as suggested by the EDX results. However, some regions of the Cr interface with Al_2O_3 do show an amorphous structure as can be seen in Fig. 3 which suggests that the work function varies on an atomic scale. Regions of amorphous Cr at the interface with Al_2O_3 can form, for example, due to the low initial temperature of the substrate in the electron-beam evaporator chamber and the high surface energy of the ALD film due to residual stress [24,25] amongst other effects that influence ordering of deposited atoms on a substrate. Variations in the work function are likely to be more important for the Au bottom electrode due to the presence of different crystal faces extended over larger areas, although the differences are expected to be small and on the order of 10 meV [26].

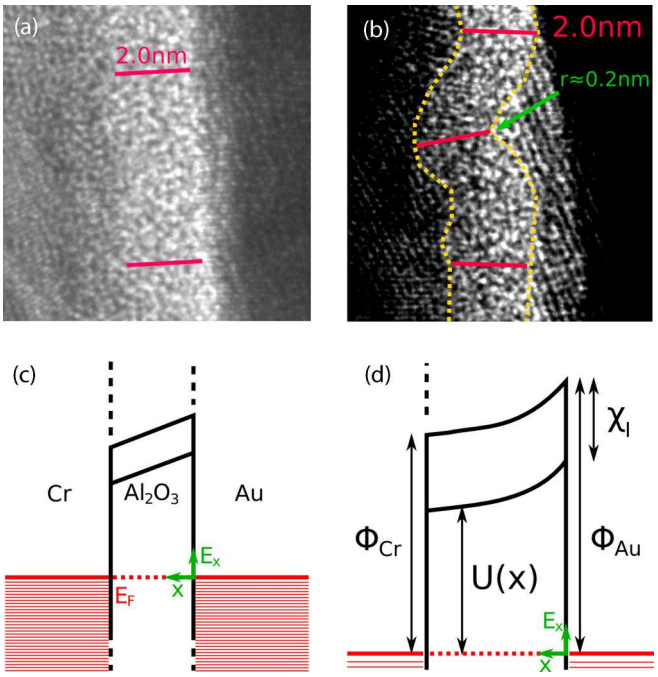

FIG. 5. (a) Flat and (b) rough regions highlighted from Fig. 3. The contrast in (b) was enhanced to distinguish the Al_2O_3 region shaded by the Cr more clearly. (c) and (d) Energy band diagrams corresponding to the situations shown in panels (a) and (b) with a uniform and distorted potential barrier, respectively. The metal work functions are denoted by $\Phi_{Au,Cr}$, the insulator electron affinity by χ_I, and $U(x)$ is the potential energy in the insulator.

Figure 5(a) and 5(b) show magnified regions of the TEM image presented in Fig. 3. From close inspection, we find two distinct types of surface features. Figure 5(a) shows a highly planar region in the MIM structure, and Fig. 5(b) an image of a region with a protruding sharp peak outlined by the dotted yellow line. The contrast in Fig. 5(b) was increased to highlight the Al_2O_3 region and the morphology of the interface.

Roughness smoothing during the deposition of amorphous layers is a well-known phenomenon. This effect is clearly illustrated in a TEM image presented by Lau *et al.* (Fig. 7 in Ref. [27]) of a symmetric device with a much thicker amorphous insulator, which shows a sharp peak on the bottom electrode. Importantly, the thickness of the insulator appears to increase near the pits to the sides of the peak on the bottom electrode in their image, and thickness uniformity normal to the peak apex is not clear. In our devices, the thickness of 2 nm measured at the peak apex appears consistent with that measured in the planar regions. However due to the small thickness of our film compared to that in Lau *et al.*'s device, it is very difficult to measure accurately the thickness fluctuations. For clarity we have outlined the interfacial boundaries in Fig. 5(b) with dotted yellow lines.

The smoothing effect can be understood as a result of the finite size of the TMA precursor molecules and the steric-hindrance-limited adsorption [28] that leads to the rounding of peak and pit features of the surface at the nanoscale, leading to thicker values of the film normal to pit features. We note that an increased thickness of the dielectric near the pit regions would decrease the tunneling probability, and the electric field would be more uniform than around peaks. Therefore, it is likely that in rough regions of the electrode small thickness fluctuations due to pits lead to a smaller current than expected in MIM devices with an insulator of uniform thickness. Furthermore, since the ALD deposited film forms a 'mould' for the surface of the top electrode, the rounded pits cause the top electrode to have smoother, slowly varying features rather than sharp crystal plane boundaries. The consequence of this is that field enhancement due to sharp features is stronger on average near the bottom electrode surface compared to the top electrode surface.

IV. FIELD-ENHANCEMENT TUNNELING MODEL

A finite element model was developed using COMSOL® to simulate and study the effect of sharp features on the bottom electrode such as those shown in Fig. 5(b). We consider a peak geometry that can be constructed using a two-dimensional model with a rotational symmetry axis as illustrated in Fig. 6(a), where r represents the peak apex radius, θ the inclination angle of the surface leading to the apex, and the green dashed line indicates the axis of rotational symmetry,

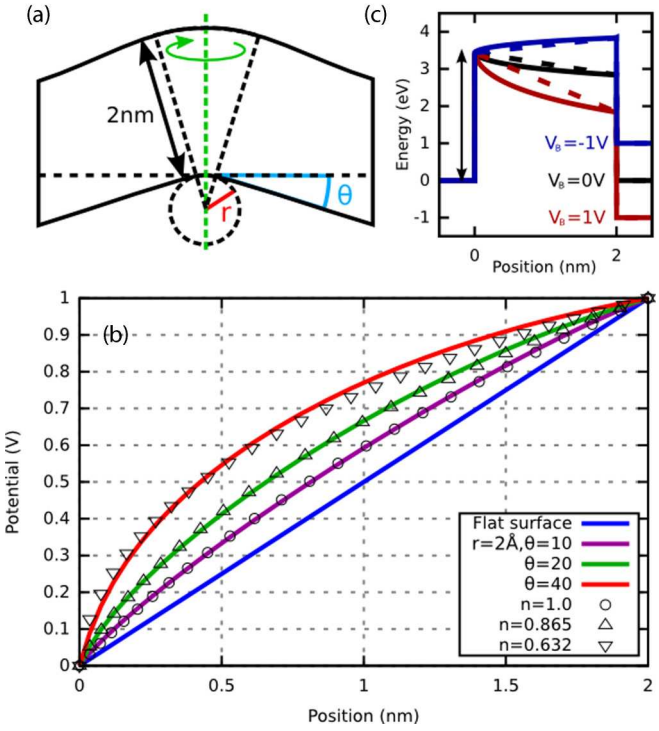

FIG. 6. (a) Geometrical model used to represent a typical peak on the bottom electrode, with the apex radius r (red), the inclination angle of the surface θ (blue), and the axis of rotational symmetry highlighted (green dashed line). (b) Potential profiles obtained for $r = 0.2$ nm as a function of the inclination angle (solid lines). Least-square fits of Eq. (1) to the potentials obtained from finite element modeling are shown as open symbols. (c) Plot showing the voltage dependence of the potential barrier using Eq. (4) and $n = 0.63$, which corresponds to $r = 0.2$ nm and $\theta = 40°$, in Eq. (1). The dashed lines represent a uniform barrier with the same material parameters. The material parameter $\chi_I = 1.66$ eV is taken from the fitting results (see below).

which is also the path along which the potential is sampled. The dielectric material is assumed to contain no free or trapped charges. For a peak radius of approximately $r = 0.2$ nm, as for the peak highlighted in Fig. 5(b), the potential profiles obtained from applying a potential difference of 1 V between the top and bottom surfaces and varying the slope angle θ are shown in Fig. 6(b) (solid lines). In the finite element model, the bottom electrode is chosen as the reference potential and is set to 0 V at position $x = 0$, corresponding to the peak apex, and the top electrode potential is set to 1 V at $x = 2$ nm. It can be seen that the potential becomes highly nonlinear as θ is increased. We note that increasing the peak radius r reduces the nonlinearity only slightly as long as the radius is smaller than the film thickness and that in this regime the nonlinearity in the potential extends far into the dielectric layer.

The spatial dependence of the potential in this model is well described by an arbitrary function of the form

$$\varphi(x) = \Delta\varphi_T \ln\left(1 + \frac{\mathrm{e} - 1}{t^n} x^n\right), \tag{1}$$

where t is the film thickness, n an arbitrary parameter, e is Euler's number, and $\Delta\varphi_T$ is the potential difference applied in the finite element model. The approximation of the potential obtained via the finite element model by this function are represented by the open symbols in Fig. 6(b). Physically realistic results are obtained when the parameter n is constrained by $n \leq 1$. When n becomes smaller than 0.5 the potential drops very rapidly near the peak apex which further restricts the parameter range in terms of physically realistic situations. The parameter n effectively represents the sharpness of the peak for small values of r (compared to t) and $\theta > 10^\circ$. For large θ, i.e. $\theta > 40^\circ$, the accuracy of the approximation decreases, however, it can still be employed for qualitative considerations. In thicker tunnel barrier systems (of the order of 5 nm for Al_2O_3) where the breakdown voltage is high enough, Fowler-Nordheim field emission dominates at voltages exceeding the barrier height, and the barrier appears triangular in shape to tunneling electrons. In this regime the precise shape of the potential barrier is very important, so field enhancement must be considered as it significantly affects the thickness of the barrier [17] as well as its average height. The approximation given above may still be used in those cases but it may not be sufficiently accurate for a precise study of the Fowler-Nordheim characteristics at high voltages.

Equation (1) must be modified to account for the work-function difference of the electrodes, and the function is then given by

$$\varphi(x) = \Delta\varphi \ln\left(1 + \frac{\mathrm{e} - 1}{t^n} x^n\right), \tag{2}$$

where $\Delta\varphi$ is the potential difference of the junction, described by

$$\Delta\varphi = V_B + \frac{\Phi_L - \Phi_R}{e}, \tag{3}$$

where V_B is the applied voltage, e is the elementary charge, and Φ_L and Φ_R represent the left and right metal electrode work functions, respectively. The spatial dependence of the potential energy in one dimension that includes any field-enhancement effects in the simplest case is then given by

$$U(x) = \Phi_L - \chi_I - e\varphi(x), \tag{4}$$

where χ_I is the insulator electron affinity, and $\varphi(x)$ the electric potential at position x in the insulator. The work-function values of these metals are widely reported; here we use the values $\Phi_{Cr} = 4.5$ eV [29,30] for the right electrode, and $\Phi_{Au} = 5.1$ eV [31] for the left electrode, corresponding to atomically clean surfaces in an abrupt contact with vacuum or an insulating material.

The voltage dependence of the potential energy barrier is shown in Fig. 6(c), which includes the potential due to the work-function difference. The dependence of the potential on the position inside the insulator considering specific surface features has been studied by others in detail [17,32,33]. Gaillard *et al.* numerically extracted interfacial roughness profiles of the top and bottom electrodes of a 45-nm-thick dielectric MIM structure using high resolution TEM images to simulate the electric field [34]. The roughness profiles in their devices are asymmetric owing to the amorphous structure of Ta_2O_5 deposited by metal-organic chemical vapor deposition (MOCVD). Their simulation results show that the electric field strength near both the interfaces can be significantly larger at protrusions but that on average the field is slightly stronger near the bottom electrode. They concluded that the asymmetry in the leakage current is possibly correlated with the asymmetric roughness profile of the interfaces. Below, we show that the model of the potential introduced above indeed yields asymmetric *IV* characteristics and that in our case the data is consistent with the interpretation of asymmetric roughness.

We now apply the approximation of the electric field described in the previous section to the calculation of the tunneling current. Figure 5(c) represents the ideal trapezoidal potential barrier [35] found where regions of the barrier are highly planar such as shown in Fig. 5(a), and Fig. 5(d) represents an example of an approximated field-enhanced potential barrier expected in regions where the bottom electrode comprises sharp features such as the one shown in Fig. 5(b). Given the large surface area of our devices, there will be variations in the fine surface features that will influence the field structure [34], but qualitative behavior at the sharpest peaks is very similar to that produced by Eq. (1) where the electric field approaches a constant value far away from a peak apex. As this approximation is applied to the description of the potential barrier it is possible to use a number of different tunneling models. Here we chose to use the Wentzel-Kramers-Brillouin-Jeffreys (WKBJ) description of the transmission probability as it is widely applied to MIM structure characterization and is the simplest model available.

Using Eq. (4), the standard WKBJ approximation [36] applied to the transmission probability of incident electrons yields

$$P_{\pm}(E_x) = \exp\left\{-\frac{2}{\hbar}\int_0^t \sqrt{2m_I(U(x) - E_x)}dx\right\} \tag{5}$$

under forward bias (+) when $V_B > 0$, where electrons incident on the barrier at $x = 0$ from the left ($x < 0$) are considered, and under reverse bias (−) when $V_B < 0$, where electrons incident on the barrier at $x = t$ from the right ($x > t$) are considered. m_I is the effective mass and E_x is the energy of incident electrons

normal to the surface, measured relative to the Fermi level of the left electrode. The current can now be calculated by adding the contributions from all regions featuring a uniform dielectric layer, and thus with a trapezoidal barrier, and contributions from all regions featuring sharp peaks in the dielectric layer, and thus with a distorted barrier. The current densities for the individual regions can be calculated using the one-dimensional version of Harrison's tunnel current density equation [37],

$$J_{\pm} = \frac{2e}{h}\int_{-\infty}^{\infty} P_{\pm}(E_x)[f(E_x) - f(E_x + eV_B)]dE_x, \quad (6)$$

where transverse wave vectors are ignored, and where $f(E)$ is the Fermi-Dirac function, defined relative to the Fermi level of the left electrode. The sign of the current is determined by the sign of the applied voltage V_B. Assuming $T = 0$ K, the integration in Eq. (6) can be performed from $-eV_B$ to 0 under forward bias (when $V_B > 0$), and from 0 to $-eV_B$ in reverse bias (when $V_B < 0$). The total current is now given by

$$I = A_i J_i + A_d J_d, \quad (7)$$

where A_i and A_d are the surface areas of the uniform regions and regions with sharp features, respectively, which are constrained by $A = A_i + A_d$, where A is the total area. J_i and J_d are the current densities associated with uniform and sharp regions, respectively, which are evaluated using Eq. (6). The parameters χ_I, m_I, A_i, A_d, and n can now be determined by fitting Eq. (7) to the experimental *IV* characteristics of the different MIM devices.

It is worth noting that this model cannot only be used to describe the effect of field enhancement due to geometrical features, but also for field enhancement induced by a local change in permittivity of the film. Under the assumption that there is no free or trapped charge, geometry-induced field enhancement produces a nonlinear flux density and electric field that are related by $D(x,V_B) = \epsilon_c \xi(x,V_B)$, where D and ξ share the same dependence on x, and ϵ_c is the constant permittivity of the dielectric. The equivalent effect can be achieved by using a position-dependent permittivity $\epsilon(x)$, so that $D(V_B) = \epsilon(x)\xi(x,V_B)$. The two interpretations can be linked through a well-behaved scaling function $f(x)$ [for example, the derivative of Eq. (1)], which in the geometrical case describes $D(x,V_B) = D(V_B)f(x)$ and $\xi(x,V_B) = \xi(V_B)f(x)$. The equivalent effect on the field can be achieved by a permittivity gradient $\epsilon(x) = \epsilon/f(x)$ which shows that the two forms are equivalent when the flux density is assumed constant in the dielectric layers. Therefore it is possible to use geometry as well as changes in permittivity to engineer the asymmetry properties of ultrathin film MIM diodes, as has been shown extensively, for example, by sequentially depositing different dielectric materials *in situ* by ALD in stacked layers [3,38] or to produce alloyed materials with new properties [1].

It is also possible that an imperfect chemistry in the first few cycles of the ALD growth may cause a permittivity gradient in certain regions due to the presence of unreacted or adsorbed compounds, which are expected to lead to optical phonons in the far-IR range. In turn, such phonons would lead to inelastic scattering of electrons, however, we could not observe any signs of inelastic scattering by computing the second derivative of the *IV* curve [39] taken at 3.7 K. We note that this could be due to the low probability of transmission of electrons in our system and insufficient adsorbates or trapped organic compounds. The nonlinearity of the *IV* curve at low voltage is a feature of a tall energetic barrier even in thinner films [38], which causes the determination of small peaks in the second derivative of the *IV* curve to be very difficult.

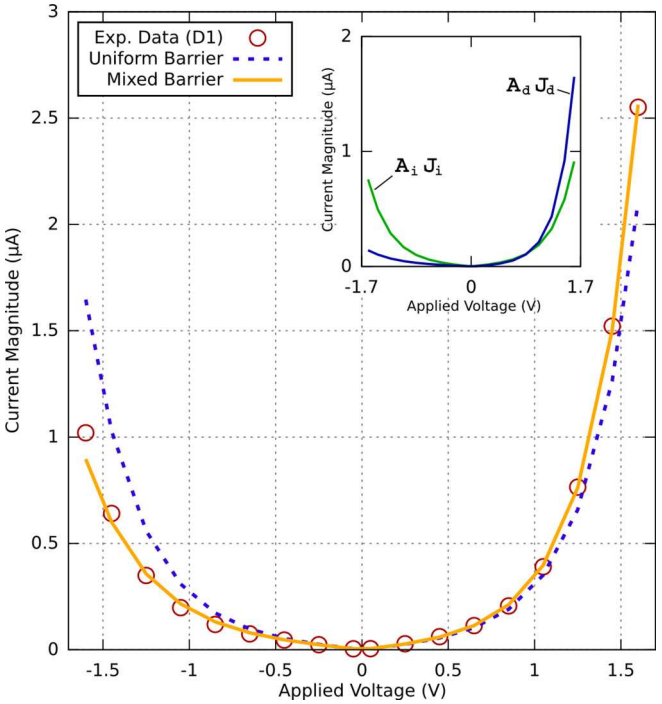

FIG. 7. Fitting results of the mixed barrier model described by Eq. (7) (solid orange line) and the uniform barrier model where $A_d = 0$ in Eq. (7) (dashed blue line), to the experimental data for device D_1 (open circles). The inset shows the two contributions to the total current.

V. RESULTS AND DISCUSSION

The results of fitting Eq. (7) to the *IV* data presented in Fig. 2 are shown in Fig. 7 and the parameters obtained are summarized in Table I. The dashed line shows the best fit ($R^2 = 0.661$) obtained when assuming a fully uniform dielectric with no sharp features, i.e., $A_d = 0$, for which we obtain the values $m_I = 0.75$ and $\chi_I = 2.03$ eV. Not surprisingly, the uniform barrier model is unable to account for the asymmetry in the *IV* data as the work-function difference alone causes only a negligible effect in the direct tunneling regime. However, when considering the effects of sharp features on the bottom electrode, the asymmetry is enhanced

TABLE I. Fitting parameter results from using Eq. (7).

Parameter	Value	Uncertainty
A_i	73% of A	±26%
A_d	27% of A	±69.5%
m_I	$0.69m_e$	±3.1%
χ_I	1.75 eV	±5.2%
n	0.83	±25.2%

TABLE II. Estimated correlations between the parameters used in the fitting process.

Parameter	m_I	n	A_i
m_I		0.967	−0.941
n	0.967		−0.994
χ_I	0.999	0.964	−0.935

by the combined effect of the work-function difference and field enhancement. This mechanism is illustrated in Fig. 6(c) where the shape of the barrier at $V_B = 0$ V (black line) is distorted due to the nonzero built-in potential. The best fit ($R^2 = 0.990$) to the model including both regions where the dielectric layer is highly uniform, as well as regions where it comprises sharp features, is represented by the solid line in Fig. 7. The inset shows the individual current components from Eq. (7). As can be seen, the asymmetry is significantly increased in field-enhanced regions, which is of interest for the design of certain MIM devices, for example IR rectennas based on MIM diodes. The uncertainty (Table I) and the correlations (Table II) in the parameters were estimated from the covariance matrix [40]. To ensure that a wide range of the parameter space is probed during fitting and to ensure the covariance matrix is representative, the starting values of the parameters were chosen to be far from the resulting optimal solution.

The correlations between the parameters obtained from the fitting are shown in Table II where a correlation of 1 between two parameters means that a change in one parameter is entirely compensated for by a positive linear change in the other. A value of −1 means the same except that changes in the two parameters are negatively linear to each other. The correlation is highest between the effective mass m_I and the affinity χ_I, which is well known to cause uncertainty when fitting IV characteristics in a limited bias voltage range [19]. Despite this, we obtained a much smaller uncertainty in these parameters than with others due to the IV curve spanning a wide voltage range so that there is an optimal solution that is stable. The reason for this can be explained by considering the squared integrand of Eq. (5), $2m_I(\Phi_L - \chi_I - e\varphi(x) - E_x)$. The relationship between m_I and χ_I can then be expressed as

$$m_I = \frac{C_1}{2(\Phi_L - \chi_I - e\varphi(x) - E_x)} = \frac{C_1}{2(C_2 - \chi_I)}, \quad (8)$$

where C_1 is a given value of the squared integrand and $C_2 = \Phi_L - e\varphi(x) - E_x$. For large values of C_2 compared to χ_I, the dependence of m_I on χ_I is quasilinear as χ_I is far away from the singularity point $\chi_I = C_2$. As the voltage is increased, at the point $x = t$ and for $E_x = 0$, the value of C_2 decreases bringing the singularity point closer to the origin which decreases the linear correlation between m_I and χ_I. With the highest voltage value used of $V_B = 1.6$ V, we find $C_2 = 2.9$ eV under forward bias which is a drastic shift from $C_2 = 4.5$ eV at $V_B = 0$ V. The other important correlation is between n and A_i (and A_d) which is not surprising as increasing n necessarily implies a decrease in A_i (and increase in A_d). The remaining correlations are less important in particular when A_d is small compared to A_i, as is illustrated above where the values of the effective mass and electron affinity are not significantly affected.

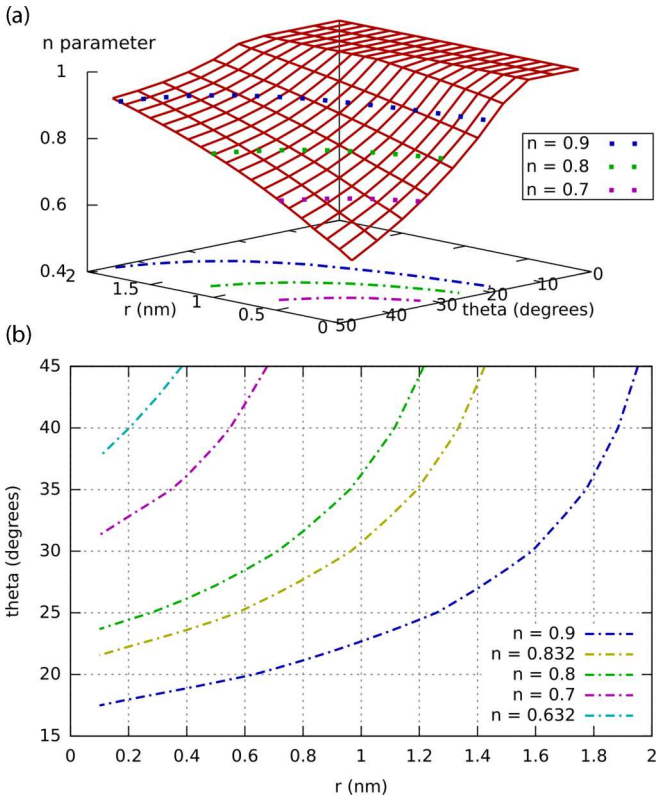

FIG. 8. (a) Parameter n from Eq. (1) as a function of r and θ obtained by fitting Eq. (1) to the data obtained via finite element modeling. The dot-dashed lines indicate the projections of the corresponding dotted lines onto the r-θ plane for selected values of n. (b) The same data as in panel (a), but showing θ as a function of r for a range of fixed n values.

The values found for the effective mass are within the range of reported experimental values, i.e., between 0.23 and 0.8 for amorphous ALD deposited Al_2O_3 [4,41–44], and theoretical predictions with values around 0.4 [45,46]. The values found for the electron affinity of Al_2O_3 are also within the range of reported values of 1.0 eV to 2.5 eV [31,47,48]. Despite the very high correlation between effective mass and electron affinity, due to the IV curve spanning a wide voltage range, there is an optimal solution that is stable for both the uniform and mixed barrier models, which is reflected in the small uncertainty in these parameters.

The value of n obtained is near the value obtained for the potential profile normal to the apex of a peak with $\theta = 20°$ and $r = 0.2$ nm, however similar potential profiles, and thus similar values of n, are obtained with different combinations of θ and r. Figure 8(a) shows the dependence of n on the possible combinations of θ and r of interest. The values of n were obtained by fitting Eq. (1) to the potential profiles obtained through finite element modeling by varying the value of r from 0.1 to 2.0 nm in steps of 0.1 nm, and the value of θ from 0 to 45° in steps of 5°. When n reaches 1, the potential is no longer well described for decreasing values of θ by a single parameter and an additional parameter may be added to Eq. (1) that extends its applicability into small θ and large r values. This is discussed in the Supplemental Material [20]. As can be seen, if θ is large the value of n is consistently smaller

than 1 even for large r values, which represents a significant distortion in the potential. Figure 8(b) shows the same data as panel (a) but here θ is shown as a function of r for a range of selected discrete values of n. From this plot it is clear that a certain n, for example as obtained in the fit to the *IV* curve, represents an infinite number of (r,θ) duplets.

We note that the value found for the area A_d appears to be large compared to the evidence revealed by the TEM images. This suggests that isolated sharp peaks are unlikely to dominate the field enhancement. In contrast, sub-nanometer-scale roughness, which may extend over a large area thus yielding a higher value of A_d, may play an important role. Since the area imaged in the TEM sample is very small compared to the area of the junction, A_d cannot be easily connected to a peak surface density without a detailed knowledge of the surface roughness over a statistically significant area. As a result, the uncertainty in the parameters A_i, A_d, and n is large. The value of n can indeed be set to a different value and a value for A_i and A_d can be found that yields a similar solution. For example, fixing $n = 0.63$, corresponding to the case identified in the TEM image, causes A_d to be reduced to 14.3% of A, while both $m_I = 0.66m_e$ and $\chi_I = 1.66$ eV remain almost unchanged, yielding a solution with an R^2 value of 0.989, hardly discernible from the optimal fit. We note that this uncertainty is due to the limited voltage range accessible in this experiment; the differences between each solution increase at very high voltages as the Fowler-Nordheim regime ($eV_B > \Phi_R - \chi_I$ in forward bias) is approached.

It is, in fact, possible to define a nonlinear potential barrier over the whole area of the junction (i.e., $A_i = 0$) which yields a solution with an R^2 value only slightly smaller than for the optimal case. The potential obtained is close to that of a uniform barrier and corresponds to the field enhancement resulting from sub-nanometer-scale roughness. Taken together these observations suggest that a more complete 'mosaic' field-enhancement model of the MIM junction may be described as

$$I(A,V_B) = \sum_{j=1}^{N} A_j J_j(V_B,n_j), \tag{9}$$

where N is the number of regions with a uniquely defined potential described by n_j covering an area A_j. While this approach is unlikely to produce unambiguous distributions of different potential profiles to model the *IV* characteristics of MIM diodes operating in the direct tunneling regime, it may be expected to produce valuable information near or in the Fowler-Nordheim regime.

We now discuss the elements of the distribution of sharp features that dominate the field enhancement to shed more light on the significance of n and A_d. We have established that a greater quantity of sharp features on the bottom electrode is due to the uniform and conformal growth of Al_2O_3 by ALD, the shape of the features on the surface and the roughness smoothing effect that occurs at the nanoscale. Although roughness smoothing is not unique to ALD, it is different to a natively grown oxide, for example, where the surface features of the bottom electrode are not preserved during oxidation by oxygen atmosphere or plasma, which leads to a more gradual interface. As the bottom electrode surface in our devices is Au, being a noble metal, the sharpest features are

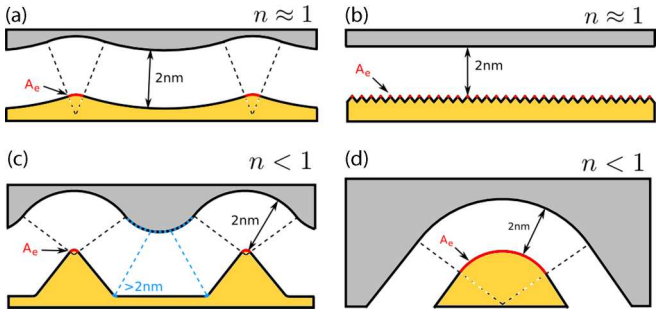

FIG. 9. Schematic representations of structures that represent areas that have a higher net field enhancement near the bottom compared to the bottom electrode. The area A_e from Eq. (10) is highlighted in red. The uniform and conformal nature of the deposited film and the roughness smoothing effect are represented but not to scale. (a) Wavelike structure characterized by large values of n with little to no net field enhancement near the bottom electrode. No roughness smoothing occurs in this idealized case. (b) Subnanoscale asymmetric roughness over a large area that, as a result of the density of the sharp peaks, is characterized by a large value of n. This is a direct consequence of the roughness smoothing effect [18,34]. (c) Isolated sharp peak structures characterized by small values of n and small area A_e. The roughness smoothing effect occurs at the base of sharp peaks. (d) An isolated, relatively blunt peak with a large area A_e and small value of n.

not altered during ALD growth and it is therefore reasonable to expect a distribution that includes atomically sharp peaks and ridges, with an abrupt interface. Figure 9 shows surfaces with different peak geometries that cause varying degrees of net field enhancement near the bottom electrode. When considering isolated three-dimensional peaks such as illustrated in Fig. 9(c), the base of the peak (highlighted in light blue) forms a ridge structure on the top electrode interface (dashed light blue) with the Al_2O_3 layer, characterized by an increased radius due to the roughness smoothing. This leads to field enhancement occurring near the top electrode in these regions, although of much smaller amplitude due to the increased thickness of the film and increased radius of the emitting surface. Similarly, large wavelike features characterized by small values of θ (<10 °) and large values of r (>0.2 nm) such as shown in Fig. 9(a) that extend over a larger scale than the thickness of the film will cause a slight field enhancement from both the top and bottom electrodes, which will mostly cancel out. In Fig. 9(b) the asymmetry in the subnanometer roughness is represented by a simple diagram. This causes stronger field enhancement near the bottom electrode on average compared to near the top electrode, as shown by Gaillard *et al.* [34]. This corresponds to a situation where there are many peaks densely packed together such that the effective field enhancement is significantly reduced compared to isolated peaks but extended over a potentially large portion of the total area.

The area A_d can be described in terms of the values of r and θ by using the model shown in Fig. 6(a). The area of the spherical cap illustrated in Fig. 9 is given by

$$A_e = 2\pi r^2(1 - \cos(\theta)), \tag{10}$$

and the potential normal to this area on the spherical surface does not change significantly. Therefore to a first approximation A_d can be written as the sum of all the contributing

instances of $A_e(r,\theta)$ from the bottom electrode, assuming that all the other contributions are small in comparison and hence can be neglected. We can see from Eq. (10) that the area increases significantly with larger r values and similarly with increasing θ. Choosing the largest value of A_e in our distribution, i.e., $r = 1.4$ nm and $\theta = 45^\circ$ obtained from the contour in Fig. 8(b), the two-dimensional density of peaks is given by $n_p = A_d/AA_e = 7.68 \times 10^{16}$ m^{-2} or one peak per 3.61 nm by 3.61 nm area of the surface when $A_d = 0.27A$. Such a high density of sharp features is not borne out of the TEM results. However, we note that it is based on a coarse approximation, which in the context of a constant thickness of the dielectric film depends on a number of contributions that will affect the result. In order of decreasing importance the following considerations will affect the resulting density of peaks: (i) the distortion in the potential extends far beyond the area A_e for isolated sharp peaks (thus increasing A_e significantly); (ii) sub-nanometer-scale densely packed peaks that extend over a large area [34] (thus effectively increasing A_e); (iii) sharp features on the surface of the top electrode which cancel out contributions from sharp features on the bottom electrode (increasing A_d); and (iv) corrections to the underestimation of A due to the assumption of a perfectly flat surface [49] (which affects all free parameters).

Furthermore, in the direct tunneling regime, the current density is strongly dependent on the thickness of the potential barrier, but fluctuations in the thickness of the film have not yet been considered. The effect of changes in thickness on the other parameters is illustrated if we assume that the thickness normal to a peak apex is reduced by 10%, i.e. 1.8 nm. If n is kept at 0.832, we find that A_d is reduced to 2.5% of A, $m_I = 0.73$ and $\chi_I = 1.85$ ($R^2 = 0.992$). With the value of $A_d = 2.5\%$ of A and following the contour for $n = 0.83$ as before yields a peak density of $n_p = 7.041 \times 10^{15}$ m^{-2} or one peak per 12 nm by 12 nm area of the surface, showing that thickness fluctuations of the film play an important role even with Å-scale fluctuations. It is very challenging to quantify such small fluctuations experimentally, in particular over large areas. In contrast, it is possible to include thickness fluctuations in our model using Miller *et al.*'s method [19], which assumes a gaussian distribution $\alpha(t)$ in the film thickness, such that $A(t) = A\alpha(t)$ is the portion of the total area with thickness t. However, experimentally identifying the parameters to describe the thickness distribution is nontrivial.

It is important to note that the effect of such small features in the surface geometry is unlikely to play a similarly important role in MIM structures comprised of electrode materials with a small electron density such as weakly doped semiconductors. The Fermi energy of electrons in metals is normally high, for bulk Au between 5 and 10 eV above the valence band edge [50–54] and for Cr on the order of 7 eV [55,56]. At kinetic energies above 1.5 eV for electrons, the de Broglie wavelength is smaller than 1 nm and, as the electron density is high, the probability of incident electrons to 'see' the fine features in the surface topography is large.

An asymmetry in the incident electron energy of the electrodes may cause a slight asymmetry in the *IV* characteristics, however, the difference in Fermi energy required is of the order of at least 5 : 1 as has been pointed out by Brinkman *et al.* [57]. In our system the Fermi energies of both Au and Cr are comparable and may contribute to the asymmetry but the effect is small. However, a detailed analysis of the band structure of the metals would be required as there are multiple subbands in the metal valence band that each present wave functions with different symmetries that may change with energy [54]. Fermi-level electrons from s-like subbands should dominate the tunneling current due the spherical character of the wave function, however other subbands such as the prominent d band in Au [58] may play a role.

Finally, we emphasise that the high consistency obtained in these devices is due to the optimal conditions for the deposition of the bottom metal electrodes and the compatibility of these electrodes with the ALD process, which allows highly uniform and conformal growth of high quality Al_2O_3. The minimal surface roughness obtained first reduces the chances the devices break down under a small applied bias and secondly the adhesion of contaminating particles should be minimized. Additionally, the surface must have had enough reactive surface sites for highly uniform growth to occur, which is likely due to the stable adsorption of atomic oxygen onto subnanoscale rough Au surfaces during the oxygen plasma exposure [21].

VI. CONCLUSION

We have shown that a high consistency in the electronic characteristics of ultrathin MIM devices can be achieved over a large area using ALD to control precisely the thickness and uniformity of the film. A highly reliable uniform thickness of 2 ± 0.1 nm was achieved for Al_2O_3 using plasma-enhanced ALD, and the tunneling current density as a function of applied electric field was found to be independent of the surface area of the MIM devices. We found that the tunnel current was strongly asymmetric, beyond what would be expected as a result of the difference in work function between the two metal electrodes. Although the dielectric thin film is highly uniform, we have shown using TEM that sharp features on the bottom metal surface lead to a net field enhancement and hence an asymmetric distortion in the potential across the film. We have developed a model which takes into account such distortions and have demonstrated that field enhancement can accurately account for the observed asymmetry in the *IV* characteristics of the MIM devices. These results show that deliberate and controlled introduction of sharp features in the metal film may be used to engineer an asymmetry and nonlinearity into the *IV* characteristics of MIM structures, which are of critical importance to a range of applications, including IR rectenna diodes, storage capacitors for DRAM, and nonvolatile memory applications.

ACKNOWLEDGMENTS

We thank Nic Hunter for assistance with cryostat systems, Michael Ward for assistance with TEM imaging, John Cunningham and Edmund Linfield for in-depth discussions. We also acknowledge Christopher Russell and Li Chen for assisting with device fabrication. We gratefully acknowledge BBSRC Grant No. BB/J012378/1 and contributions from the Hitachi Cambridge Laboratory and support from the Royal Society and Wolfson Foundation. Data supporting this work can be accessed via the University of Leeds Data Repository [59].

[1] H. Hu, C. Zhu, X. Yu, A. Chin, M. F. Li, B. J. Cho, D.-l. Kwong, P. D. Foo, M. B. Yu, X. Liu, and J. Winkler, IEEE Electron Device Lett. **24**, 60 (2003).

[2] Q.-X. Zhang, B. Zhu, S.-J. Ding, H.-L. Lu, Q.-Q. Sun, P. Zhou, and W. Zhang, IEEE Electron Device Lett. **35**, 1121 (2014).

[3] I. E. Hashem, N. H. Rafat, and E. A. Soliman, IEEE J. Quantum Electron. **49**, 72 (2013).

[4] N. Alimardani, E. William Cowell, J. F. Wager, J. F. Conley, D. R. Evans, M. Chin, S. J. Kilpatrick, and M. Dubey, J. Vac. Sci. Technol. A **30**, 01A113 (2012).

[5] R. W. Johnson, A. Hultqvist, and S. F. Bent, Mater. Today **17**, 236 (2014).

[6] M. Bareiß, A. Hochmeister, G. Jegert, U. Zschieschang, H. Klauk, R. Huber, D. Grundler, W. Porod, B. Fabel, G. Scarpa, and P. Lugli, J. Appl. Phys. **110**, 044316 (2011).

[7] A. Mayer, M. S. Chung, P. B. Lerner, B. L. Weiss, N. M. Miskovsky, and P. H. Cutler, J. Vac. Sci. Technol. B **30**, 031802 (2012).

[8] P. Periasamy, H. L. Guthrey, A. I. Abdulagatov, P. F. Ndione, J. J. Berry, D. S. Ginley, S. M. George, P. a. Parilla, and R. P. O'Hayre, Adv. Mater. **25**, 1301 (2013).

[9] K. K. Likharev, Proc. IEEE **87**, 606 (1999).

[10] K. K. Yadavalli, A. O. Orlov, G. L. Snider, and J. Elam, Microelectron. J. **36**, 272 (2005).

[11] H. C. George, A. O. Orlov, and G. L. Snider, J. Vac. Sci. Technol., B: Microelectron. Nanometer Struct. **28**, C6L6 (2010).

[12] N. S. Bakhvalov and K. K. Likharev, Sov. Phys. JETP **68**, 581 (1989).

[13] P. S. Davids, R. L. Jarecki, A. Starbuck, D. B. Burckel, E. A. Kadlec, T. Ribaudo, E. A. Shaner, and D. W. Peters, Nat. Nanotechnol. **10**, 1033 (2015).

[14] S. Grover, S. Member, G. Moddel, and S. Member, IEEE Journal of Photovoltaics **1**, 78 (2011).

[15] K. Bordo and H.-G. Rubahn, Mater. Sci. **18**, 313 (2012).

[16] J. Zhang, M. Irannejad, M. Yavuz, and B. Cui, Nanoscale Res. Lett. **10**, 238 (2015).

[17] R. G. Forbes, Nanotechnology **23**, 095706 (2012).

[18] W. S. Lau, J. Zhang, X. Wan, J. K. Luo, Y. Xu, and H. Wong, AIP Adv. **4**, 027120 (2014).

[19] C. W. Miller, Z.-P. Li, J. Akerman, and I. K. Schuller, Appl. Phys. Lett. **90**, 043513 (2007).

[20] See Supplemental Material at http://link.aps.org/supplemental/10.1103/PhysRevB.96.115435 for additional images and supporting data.

[21] T. A. Baker, C. M. Friend, and E. Kaxiras, J. Phys. Chem. C **113**, 3232 (2009).

[22] K. Okazaki-Maeda and M. Kohyama, Chem. Phys. Lett. **492**, 266 (2010).

[23] "Eels atlas", http://www.eels.info/atlas, accessed: 2016-12-01.

[24] C. A. Neugebauer, *Handbook of Thin Film Technology*, edited by L. I. Maissel and R. Glang (McGraw-Hill, New York, USA, 1970), Chap. 8, pp. 8-31–8-32.

[25] O. M. E. Ylivaara, X. Liu, L. Kilpi, J. Lyytinen, D. Schneider, M. Laitinen, J. Julin, S. Ali, S. Sintonen, M. Berdova, E. Haimi, T. Sajavaara, H. Ronkainen, H. Lipsanen, J. Koskinen, S. P. Hannula, and R. L. Puurunen, Thin Solid Films **552**, 124 (2014).

[26] G. V. Hansson and S. A. Flodström, Phys. Rev. B **18**, 1572 (1978).

[27] W. S. Lau, D. Q. Yu, X. Wang, H. Wong, and Y. Xu, in *Semiconductor Technology International Conference (CSTIC), 2015 China* (IEEE, Shanghai, China, 2015), pp. 1–3.

[28] R. L. Puurunen, J. Appl. Phys. **97**, 121301 (2005).

[29] J. J. Attema, M. A. Uijttewaal, G. A. de Wijs, and R. A. de Groot, Phys. Rev. B **77**, 165109 (2008).

[30] A. J. Hong, J. Kim, K. Kim, Y. Wang, F. Xiu, J. Jeon, J. Park, I. Rauda, L. M. Chen, Y. Yang, S. Tolbert, J. Zou, and K. L. Wang, J. Appl. Phys. **110**, 054504 (2011).

[31] Y. C. Yeo, T. J. King, and C. Hu, J. Appl. Phys. **92**, 7266 (2002).

[32] M. V. Krylov and R. A. Suris, Sov. Phys. JETP **61**, 1303 (1985).

[33] K. Choi, F. Yesilkoy, G. Ryu, S. H. Cho, N. Goldsman, M. Dagenais, and M. Peckerar, IEEE Trans. Electron Devices **58**, 3519 (2011).

[34] N. Gaillard, L. Pinzelli, M. Gros-Jean, and A. Bsiesy, Appl. Phys. Lett. **89**, 133506 (2006).

[35] A. Modinos, G. C. Aers, and B. V. Paranjape, Phys. Rev. B **19**, 3996 (1979).

[36] R. G. Forbes, J. Appl. Phys. **103**, 114911 (2008).

[37] W. A. Harrison, Phys. Rev. **123**, 85 (1961).

[38] M. Alhazmi, F. Aydinoglu, B. Cui, O. M. Ramahi, M. Irannejad, A. Brzezinski, and M. Yavuz, Austin Journal of Nanomedicine & Nanotechnology **2**, 4 (2014).

[39] J. Lambe and R. C. Jaklevic, Phys. Rev. **165**, 821 (1968).

[40] M. Newville, T. Stensitzki, D. B. Allen, and A. Ingargiola, (2014), doi: 10.5281/zenodo.11813.

[41] S. Y. No, D. Eom, C. S. Hwang, and H. J. Kim, J. Electrochem. Soc. **153**, F87 (2006).

[42] K. B. Jinesh, J. L. van Hemmen, M. C. M. van de Sanden, F. Roozeboom, J. H. Klootwijk, W. F. A. Besling, and W. M. M. Kessels, J. Electrochem. Soc. **158**, G21 (2011).

[43] E. W. Cowell, S. W. Muir, D. A. Keszler, and J. F. Wager, Jpn. J. Appl. **114**, 213703 (2013).

[44] K. El Hajjam, N. Baboux, F. Calmon, A. Souifi, O. Poncelet, L. A. Francis, S. Ecoffey, and D. Drouin, J. Vac. Sci. Technol. A **32**, 01A132 (2014).

[45] Y. Yourdshahyan, C. Ruberto, L. Bengtsson, and B. Lundqvist, Phys. Rev. B **56**, 8553 (1997).

[46] T. V. Perevalov, V. A. Gritsenko, and V. V. Kaichev, Eur. Phys. J.: Appl. Phys. **52**, 30501 (2010).

[47] M. L. Huang, Y. C. Chang, C. H. Chang, T. D. Lin, J. Kwo, T. B. Wu, and M. Hong, Appl. Phys. Lett. **89**, 012903 (2006).

[48] N. Alimardani and J. F. Conley, Appl. Phys. Lett. **105**, 082902 (2014).

[49] L. Lai and E. A. Irene, J. Vac. Sci. Technol. B **17**, 33 (1999).

[50] G. M. Ramchadani, J. Phys. C: Solid State Phys. **3**, S1 (1970).

[51] C. Fadley and D. Shirley, J. Res. Natl. Bur. Stand., Sect. A **74A**, 543 (1970).

[52] K. Liang and W. Salaneck, Solid State Commun. **19**, 329 (1976).

[53] T. Rangel, D. Kecik, P. E. Trevisanutto, G.-M. Rignanese, H. Van Swygenhoven, and V. Olevano, Phys. Rev. B **86**, 125125 (2012).

[54] B. Yan, B. Stadtmüller, N. Haag, S. Jakobs, J. Seidel, D. Jungkenn, S. Mathias, M. Cinchetti, M. Aeschlimann, and C. Felser, Nat. Commun. **6**, 10167 (2015).

[55] J. L. Fry, N. E. Brener, J. L. Thompson, and P. H. Dickinson, Phys. Rev. B **21**, 384 (1980).

[56] P. E. S. Persson and L. I. Johansson, Phys. Rev. B **34**, 2284 (1986).

[57] W. F. Brinkman, J. Appl. Phys. **41**, 1915 (1970).

[58] A. Sekiyama, J. Yamaguchi, A. Higashiya, M. Obara, H. Sugiyama, M. Y. Kimura, S. Suga, S. Imada, I. A. Nekrasov, M. Yabashi, K. Tamasaku, and T. Ishikawa, New J. Phys. **12**, 043045 (2010).

[59] L. Fry-Bouriaux, M. C. Rosamond, D. A. Williams, A. G. Davies, and C. Wälti, "Dataset associated with the publication: Field-enhanced direct tunneling in ultra-thin ALD-grown Au-Al2O3-Cr MIM structures", https://doi.org/10.5518/238 (2017).